Nonlinear Dynamics manuscript No.
(will be inserted by the editor)

State-space realization of a describing function

Giulio Ghirardo · Bernhard Ćosić · Matthew P. Juniper · Jonas P. Moeck

Received: date / Accepted: date

Abstract The describing function is a powerful tool to characterize nonlinear dynamical systems in the frequency domain. In some cases, it is the only available description of a nonlinear operator characterizing a certain subcomponent of the system. This paper presents a methodology to provide a state-space realization of one given describing function, in order to allow the study of the system in the time domain as well. The realization is based on Hammerstein models and Fourier–Bessel series. It can be embedded in time domain simulations of complex configurations with many nonlinear elements interacting, accurately describing the nonlinear saturation of the system. The technique is applied to an example application in the field of combustion instability, featuring self-excited thermoacoustic oscillations. We benchmark the performance of the tool comparing the results with a frequency domain analysis of the same system, obtaining good agreement between the two formulations.

Keywords describing function · state-space realization · time domain · thermoacoustic networks

1 Introduction

Combustion systems are subject to acoustic fluctuations of pressure and velocity, called thermoacoustic oscillations [1,2]. These arise from the interaction between acoustic waves and the unsteady heat release rate from the flame, which locally induces a gas expansion. Often these systems are not globally stable, and can nonlinearly saturate to a dynamic attractor, which in most cases is a time-periodic acoustic field.

An increasingly large number of experiments [3,4,5,6,7] and numerical simulations [8,9,10,11] investigate the nonlinear response of the unsteady heat release rate to sinusoidal acoustic forcing. The same can be done for Helmholtz resonators [12,13,14], which are acoustic damping devices. In particular, both elements (flame and Helmholtz resonator) can be isolated to an open-loop configuration, and forced by a harmonic input at a fixed frequency and amplitude: for the flame, the input is an acoustic longitudinal velocity fluctuation just upstream of the flame; for the resonator, the input is an acoustic pressure fluctuation at the interface between the neck of the resonator and the encasing geometry. Both elements are assumed to be stable, time-invariant operators, so that the output signal has the same period of the input. The response is measured in terms of the gain and of the phase difference between output and input. This is the sinusoidal-input describing function [15] of the element, from here onwards referred to simply as the describing function.

One can then study the element in a closed-loop configuration, which in the case of thermoacoustics corresponds to placing it in an enclosing geometry, which feeds back the output of the element as the input (reflection of acoustic waves). If the system undergoes a Hopf bifurcation, one can then track the stability of the whole system as a function of the amplitude of the limit cycle, by applying harmonic balance truncated at the first harmonic. The technique is succinctly described in [16], and works quite well as long as the system acts as a low-pass filter on the higher-order harmonics, commonly known as the filtering hypothesis.

G. Ghirardo · M.P. Juniper
Department of Engineering, University of Cambridge, Trumpington Street, Cambridge CB2 1PZ, UK
E-mail: giulio.ghirardo@gmail.com

B. Ćosić · J.P. Moeck
TU Berlin, Mller-Breslau-Strae 8, D-10623 Berlin

Difficulties arise if, for certain parameters, more than one mode of self-sustained oscillation is possible, because the knowledge of the describing function to multiple inputs is then required, as discussed for thermoacoustic systems in [17,18].

A second difficulty regards the onset of a secondary bifurcation, often of the Neimark-Sacker type, where 2 distinct frequencies emerge, as found in experiments by [19] and in numerical simulations [20] (not yet published). This can still be discussed within the describing function framework [16,21], but is not be considered in this article.

A third difficulty arises in the low-order modelling of thermoacoustic oscillations in annular combustors, where the geometric discrete rotational symmetry makes the system's linearized dynamics degenerate: a 2-dimensional eigenspace becomes linearly unstable at a double Hopf bifurcation[1], i.e. 2 complex conjugate pairs of eigenvalues sharing the same frequency and growth-rate cross the imaginary axis at the same time. To tackle this third difficulty, a state-space formulation of the problem is proposed for annular geometries by [22]. One can then study the dynamical system, either with time-integration, numerical-continuation, or analytically with the method of averaging [23] or of multiple scales [24]. The major drawback of these state-space investigations (see also [25,26,27]) is that the description of the flame response in state-space has so far been phenomenological and not quantitative.

Section 2 of this paper presents a quantitative state-space realization of one given describing function, so that it can be used in time domain models of thermoacoustic systems. This modelling tool can improve the industrial design process, by predicting the nonlinear frequency shift of a mode when compared to a linear analysis, and correctly modelling the softening [14] of Helmholtz resonators in the nonlinear regime.

Note that the focus here is not on system identification, because the system is fully described in the frequency domain[2], and time domain input/output data are often not available. [28] describes qualitatively the inversion of a describing function, for the purpose of controlling a nonlinear system. [29] describes an iterative, numerical algorithm to calculate a nonlinear saturation function for a given real-valued describing function. We propose here instead a Fourier–Bessel series decomposition, which allows the calculation of a good fit without requiring iterations. This is based on the analytic evaluation of the describing function of a Fourier–Bessel term, discussed in appendix A. This procedure is of general applicability and has good convergence properties in all cases studied (see for example figure 5). The nonlinear saturation is then used as part of a modified Hammerstein model [30], pictured in figure 2.b. This allows us to model the dependence of the phase response on the input amplitude, so that also a complex-valued describing function can be fitted. Section 2 discusses how to fit accurately first the linear part of the model and then the nonlinear part.

To show the applicability of this nonlinear state-space realization, we study in section 3 an example problem modelling a self-excited thermoacoustic experiment [7], which depends on a geometric parameter L of the configuration (the length of the combustion chamber). We then study the system parametrically in L with 2 methods.

The first method consists of a first-order harmonic balance method, often described in thermoacoustics as the flame describing function framework [4]. It predicts the amplitudes and the frequencies of the limit cycles as function of L, as presented in figure 9.

The second method is the time domain realization of the system, using the state-space realization of the describing function described in section 2. We run time domain simulations of the problem and extract the amplitude and the frequency of the dominant harmonic of the signal. One example of simulation is presented in figure 11.

We then compare the results of the 2 methods in section 3.3, obtaining a good match, and discuss the accuracy of the time domain model.

We finally discuss the applications of this methodology and possible improvements in section 4.

2 The state-space realization

The describing function represents the response of a nonlinear operator $\mathcal{Q}[u(t)]$ to a sinusoidal input $u(t) = A\cos(\omega t)$. In our application u is the fluctuating velocity measured upstream of the flame, just downstream of the burner, with amplitude A and forcing frequency ω, and the quantity $\mathcal{Q}$ describes the fluctuating heat release rate measured at the flame. This section is, however, general, and applies to a generic single-input single-output (SISO) system. The describing function of the operator $\mathcal{Q}$ is defined [15] as

$$Q(A,\omega) = \frac{1}{A}\frac{1}{\pi/\omega}\int_0^{2\pi/\omega} \mathcal{Q}\left[A\cos(\omega t)\right] \left(\cos(\omega t) + i\sin(\omega t)\right) dt \quad (1)$$

[1] many annular combustors are also slightly not-axisymmetric, perturbing this double-Hopf bifurcation

[2] To be precise the response is defined at discrete values of frequency and amplitude, and then interpolated inbetween.

As a matter of nomenclature, we will use capital letters to indicate the describing or transfer function of an operator, such as $Q(A,\omega)$, and we will use capital calligraphic letters to describe the corresponding time domain operator, such as $\mathcal{Q}[u(t)]$. The quantity $Q(A,\omega)$ is a complex number, with its real and imaginary parts expressing the amplitudes of the components of $\mathcal{Q}$ respectively in phase and in quadrature with the sinusoidal input. One can then define the gain G and the phase φ of the flame response as the polar coordinates of the complex number $Q(A,\omega)$:

$$Q(A,\omega) = G(A,\omega)e^{i\varphi(A,\omega)},\ G,\varphi : \mathbb{R}^+ \times \mathbb{R}^+ \mapsto \mathbb{R} \tag{2}$$

$$\begin{cases} G(A,\omega) &= |Q(A,\omega)| \\ \varphi(A,\omega) &= \arg[Q(A,\omega)] \end{cases} \tag{3}$$

We assume that the function $Q(A,\omega)$ is provided over the range of frequencies and amplitudes of interest, from data coming from experiments, numerical simulations or analytical models. To provide an example of the application of this technique, we apply it to an experiment carried out by [31,7]. The describing function of the heat release rate response is shown in figure 1. It has been gently smoothed from experimental data using B-splines [32]. In addition, the phase is unwrapped by 2π to present a continuous function $\varphi(A,\omega)$ in the domain.

We want to provide a state space model that is equivalent to the given describing function. Notice that the describing function provides information on how the system behaves if only one fundamental harmonic is present. In the same way, the state space model will be accurate as long as the system presents a strong fundamental harmonic. This restricts the applicability to the describing function framework, and will accurately describe the state of the system if, after the Hopf bifurcation, secondary bifurcations do not occur. The model will be tuned at a design frequency ω_d, at which it will be most accurate. For example, one can choose as design frequency the frequency of the least stable mode of the whole system, obtained from a linear stability analysis. One can then run the time simulation, and let the system evolve to a saturated limit cycle, with a nonlinear saturated frequency $\omega_{d,1} = \omega_d + \Delta\omega$. If $\Delta\omega$ is large, one can tune the flame model to the frequency $\omega_{d,1}$ and either run a second time simulation or continue from the first limit cycle.

Figure 2 shows a sketch in the complex plane of the input and of the output phasors[3] of the describing function, at a fixed design frequency ω_d. The sinusoidal inputs $Ae^{i\omega_d t}$ rotate in time in the anticlockwise direction, for 3 different amplitudes A, in the top-left quadrant (the other features of the figure are discussed in the next section). The input is operated on by $\mathcal{Q}$ and the subsequent output is shown in the top-right quadrant. Since $\mathcal{Q}$ is a fully nonlinear operator, the phase and the gain responses depend on the amplitude A, and the 3 output phasors are not parallel, nor is the ratio of their moduli with the respective input moduli constant.

In subsection 2.1 and 2.2 we choose the structure of the state-space realization. The following subsections 2.3 and 2.4 carry out the fitting of respectively the linear and nonlinear elements that define the realization. Subsection 2.5 briefly summarizes this section.

2.1 Operator splitting

We decompose the heat release rate response as the sum of 2 nonlinear operators, as represented in figure 2.b

$$\mathcal{Q}[u(t)] = \mathcal{Q}_-[u(t)] + \mathcal{Q}_+[u(t)] \tag{4}$$

$$\begin{cases} Q_-(A,\omega) = & G_-(A,\omega)e^{i\varphi_-(A,\omega_d)} \\ Q_+(A,\omega) = & G_+(A,\omega)e^{i\varphi_+(A,\omega_d)} \end{cases} \tag{5}$$

The reasoning behind this choice is that the 2 operators $\mathcal{Q}_-$ and $\mathcal{Q}_+$ will be designed to have a constant phase response with amplitude. This feature will allow us to model each of them as a Hammerstein block in section 2.2. The frequency ω_d in (5) is the frequency at which the time domain realization will be most accurate. We design the 2 operators to have phase responses that differ by $\pi/2$, as can be observed in figure 2.a where their phase responses (dashed black arrows) are orthogonal. Their phase response is defined as:

$$\begin{cases} \varphi_-(A,\omega) & \equiv \varphi(A,\omega) - \varphi(A,\omega_d) + \overline{\varphi}_d - \pi/4 \\ \varphi_+(A,\omega) & \equiv \varphi(A,\omega) - \varphi(A,\omega_d) + \overline{\varphi}_d + \pi/4 \end{cases} \tag{6}$$

From the definition (6) the output signals of the 2 operators are always in quadrature, and they are defined so that at the design frequency ω_d they present the phases

$$\varphi_-(A,\omega_d) = \overline{\varphi}_d - \pi/4 \tag{7a}$$

$$\varphi_+(A,\omega_d) = \overline{\varphi}_d + \pi/4 \tag{7b}$$

The design phase $\overline{\varphi}_d$ is the green (negative) angle between the input (vectors in the top-left quadrant) and the dashed line in the top-right quadrant in figure 2. The value of $\overline{\varphi}_d$ is quite arbitrary, though in most cases it is chosen as the mean phase response with amplitude of the operator $\mathcal{Q}$ at the design frequency ω_d; secondary considerations on the limitations of this choice are discussed at the end of section 2.3. The 2 operators have

[3] a phasor is a representation of a sinusoidal function with a certain amplitude, frequency and phase in the complex plane

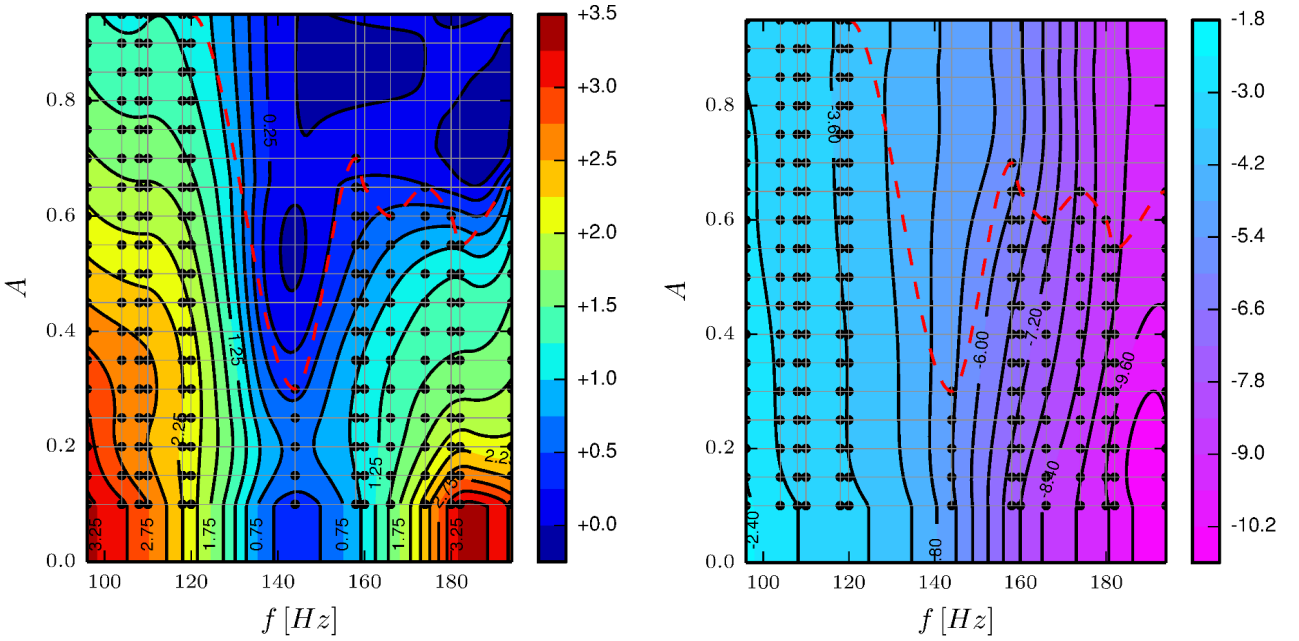

(a) Gain response

(b) Phase response

Fig. 1: Smoothed, interpolated data coming from the experiment. The black dots are individual experiments, carried out at a fixed frequency (horizontal axis, in Hz) and forcing velocity amplitude (vertical axis, normalized with respect to the mean upstream velocity). The red dashed line is the curve below which the interpolation is valid, because above it no experimental data is available. At velocity amplitudes below the minimum tested velocity the corresponding value was used (at the bottom of both plots).

then a phase response that is shifted of $\pm\pi/4$ with respect to that dashed line, as defined in (6). Once $\overline{\varphi}_d$ is fixed, the phase response of the 2 operators is fixed too by (6), and the 2 gains $G_{\mp}(A,\omega)$ can be calculated from (4). In other words, the original operator $\mathcal{Q}$ is rewritten as the sum of its 2 projections on these 2 directions. The projections are shown in figure 2 with red, orange, yellow colours.

2.2 Nonlinear saturation

This subsection applies in the same way to each of the operators $\mathcal{Q}_-$ and $\mathcal{Q}_+$. For ease of notation, we drop the subscript $\pm$ here. We express each of the operators $\mathcal{Q}$ as the composition of a linear operator $\mathcal{L}$ and a nonlinear operator $\mathcal{N}$, as presented in figure 2.b. We choose as linear operator the linearization of $\mathcal{Q}$:

$$L(\omega) \equiv Q(0,\omega) \tag{8}$$

In (8), L is a transfer function, since it does not depend on the amplitude by definition. The composition of $\mathcal{L}$ and $\mathcal{N}$ can happen in 2 ways [33]:

$$\text{Wiener model} \qquad \mathcal{Q} = \mathcal{N}\Big[\mathcal{L}\big[u(t)\big]\Big] \tag{9a}$$

$$\text{Hammerstein model} \qquad \mathcal{Q} = \mathcal{L}\Big[\mathcal{N}\big[u(t)\big]\Big] \tag{9b}$$

We now briefly discuss which model is best suited for the problem at hand. The 2 options lead to a different expression for the describing function N:

$$\text{Wiener} \qquad N_{NL}(A,\omega) = Q\Big(\frac{A}{|Q(0,\omega)|},\omega\Big)/Q(0,\omega)$$

$$\text{Hammerstein} \qquad N_{LN}(A,\omega) = Q(A,\omega)/Q(0,\omega)$$

We present in figure 3 the gains of N_{NL} and N_{LN} applied to the full operator Q introduced in (1) (the same considerations apply when considering Q_- and Q_+). Because of (8), the gains are unity at zero amplitude A, as discussed in [30]. Each curve represents the nonlinear saturation with the amplitude A of the input at a fixed frequency, with the color of the line indicating the frequency value. We observe that in the case 3.b the nonlinear saturation curves have a weak dependence on the frequency, and tend to overlap better, especially at large amplitudes. This happens because the dominant factor of the nonlinear saturation is the amplitude of

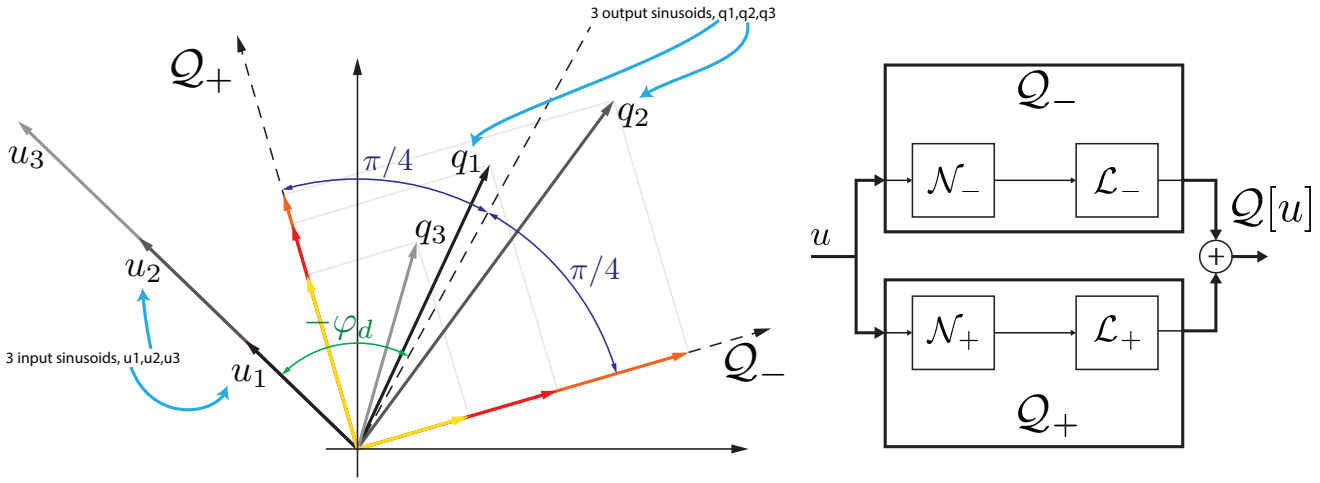

(a) phasor space representation (b) flowchart representation

Fig. 2: a) Representation of the input and output phasor of the nonlinear operator in the complex plane at the design frequency ω_d at one instant in time. The 3 black, gray and light gray arrows in the top-left quadrant represent 3 input phasors with increasing amplitude. These phasors rotate around the origin in time, with direction $e^{i\omega_d t}$. The output phasors are represented with the three grayscale thick arrows in the top-right quadrant. The gain and the phase of the output depend on the input amplitude, e.g. the 3 thick phasors in the top-right quadrant are not parallel. The mean phase response $\overline{\varphi}_d$ of the outputs subtends the arc. The 2 nonlinear operators $Q_\pm$ are designed so that their phase response is $\pm\pi/4$ the mean phase response $\overline{\varphi}_d$. The 2 dashed black arrows are the directions of the 2 operators. The output phasor is then calculated as the sum of its projections onto the 2 operators. The projections at the 3 amplitudes are the red, orange and yellow arrows. b) block diagram of the model. The internal structure of each of the operators $\mathcal{Q}_\pm$ is a Hammerstein model, discussed in section 2.1

forcing, and not the amplitude of the linear response. This is a feature of forced flames, where one leading nondimensional number governing the saturation is the ratio $A/\overline{U}$, with $\overline{U}$ the bulk velocity at the burner inlet.

We must also take into account that the nonlinear operator $\mathcal{N}$ produces, as output, spurious odd harmonics of the input frequency. These harmonics do not hold any meaning, and can be filtered out with the structure (9b) if $\mathcal{L}$ behaves like a low-pass filter outside the range of frequencies studied. This is a feature of flames [34] and a necessity for the model to work, as we want to comply with the hypothesis of strong attenuation of higher harmonics that characterizes the describing function framework. We therefore opt for the Hammerstein model described by (9b).

We now exploit the weak dependence of the gain of N on the frequency, and choose for N a static, i.e. memory-less, nonlinearity. By operating in this way, the linear operator $\mathcal{L}$ depends only on the frequency, and the nonlinear operator $\mathcal{N}$ depends only on the amplitude:

$$\mathcal{Q} = \mathcal{L}\Big[\mathcal{N}\big[u(t)\big]\Big] \qquad Q(A,\omega) = N(A)L(\omega) \tag{10}$$

In the frequency domain, we are then approximating

$$Q(A,\omega) \approx N_-(A)L_-(\omega) + N_+(A)L_+(\omega) \tag{11}$$

and we will make this approximation accurate at the design ferquency ω_d. Section 2.3 discusses how to calculate the linear operators $\mathcal{L}_\pm$, and section 2.4 discusses how to calculate the nonlinear operators $\mathcal{N}_\pm$.

2.3 Linear operator fitting

We want to calculate a fit for the linear operator $\mathcal{L}$, whose frequency response along the imaginary axis $s = i\omega$ is defined by equation (8). We choose to fit this curve with rational function approximations, as discussed by [35,36]. In particular, the transfer function of the operator is fitted to

$$\mathcal{L}^{\text{fit}}(s) = \sum_{n=1}^{N} \frac{c_n}{s - a_n} + d\ , \qquad s = \sigma + i\omega \tag{12}$$

where $\{c_n, a_n\}$ and d are the coefficients of the fit, which were calculated using the package VFIT3 written by [36]. This is quite an established technique, used for example in [37] to run time domain simulation of a linear system, and in [38] to identify and simulate components

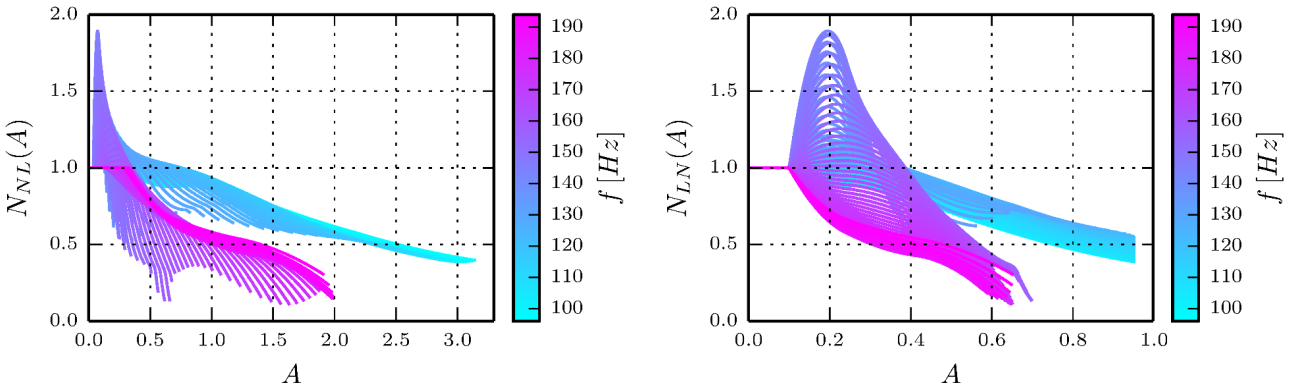

(a) Nonlin. sat. of the Wiener model

(b) Nonlin. sat. of the Hammerstein model

Fig. 3: Slices of the nonlinear gain $G(A,\omega)$ at 100 frequencies, equispaced from 96 Hz to 194 Hz. Each line corresponds to a different frequency, associated to a different color on the colorbar on the right. In (a) the gain of the operator $\mathcal{N}$ is applied after the operator $\mathcal{L}$ as in (9a), and this results in larger amplitudes A. In (b) the operator $\mathcal{N}$ is applied before the operator $\mathcal{L}$ as in (9b). 2 main behaviours are found around 2 distinct frequencies, corresponding to the 2 hills in the describing function of figure 1 around 100 Hz and around 190 Hz. The saturation curves are closer in (b).

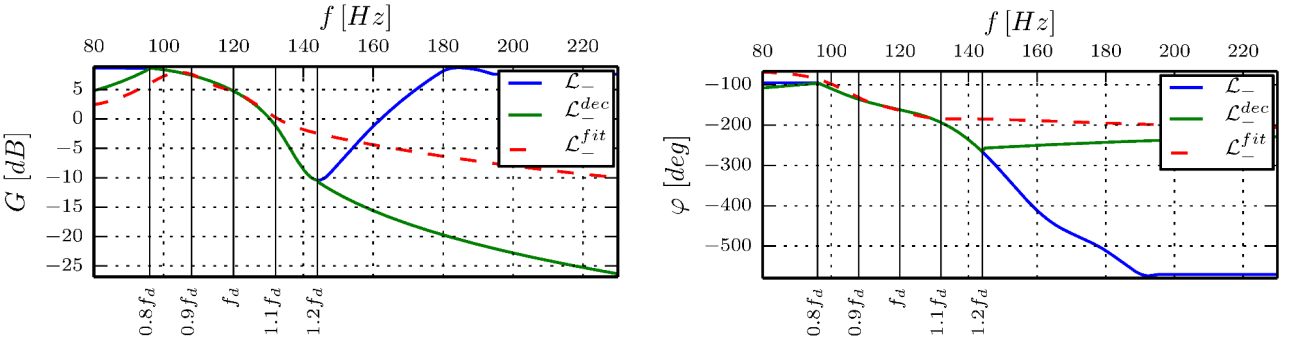

(a) Gain response

(b) Phase response

Fig. 4: Fitting at f_d =120 Hz of the linear operator $\mathcal{L}_-$. The gain is decreased outside the range $[0.8\omega_d, 1.2\omega_d]$. The fit is then weighted higher in the range $[0.9\omega_d, 1.1\omega_d]$, where the fit is more accurate.

of acoustic and thermoacoustic systems. In this case, we enforce the stability of the linear operator, but do not enforce a passivity constraint [39].

The tool VFIT3 also calculates the matrices A, B, C, D that describe the state-space realization of (12):

$$\dot{x} = Ax + Bu \tag{13a}$$

$$y = Cx + Du \tag{13b}$$

where x is a vector variable describing the internal state, and u and y are respectively the scalar input and output of the linear operator.

An important parameter of the fitting is the number N of poles in (12). A large number N usually leads to smaller errors within the range of frequencies $[\omega_1, \omega_2]$ at which data is available. On the other hand, a large N usually results in a fit with many poles a_n outside the range $[\omega_1, \omega_2]$. These in turn lead to large, unphysical gains outside of the range of frequencies $[\omega_1, \omega_2]$ studied, violating our requirement of a low-pass filter behavior at the higher frequencies. This is often referred to as overfitting [40], and if overlooked can lead to strongly oscillating time domain simulations at very high frequencies.

Because of these considerations and after some testing, we choose a number of $N = 8$ poles to do the fitting. We observe that we need: *1)* a low-pass filter behavior at the frequencies of the higher order harmonics, i.e. at $(2k+1)\omega_d$, $k \in \mathbb{N}_{>0}$, as discussed in section 2.2; *2)* an accurate fit only in the vicinity of the design frequency ω_d;

To satisfy the first constraint, we extend the fit to a broader range of frequencies, from 30 Hz to 776 Hz. Moreover, outside the range $[0.8\omega_d, 1.2\omega_d]$ we make the gain decrease towards zero. This guarantees that the fit will be well behaved outside the range of frequencies of interest, i.e. it will not exhibit unexpected large gains due to overfitting.

To satisfy the second constraint, we provide to the fitting tool VFIT3 a vector of weights, which we choose larger in the range $[0.9\omega_d, 1.1\omega_d]$ to improve the accuracy in a neighbourhood of ω_d.

We present an example of the fitting in figure 4, where the original response $\mathcal{L}$, the decreased response $\mathcal{L}^{\text{dec}}$ and the fitted operator $\mathcal{L}^{\text{fit}}$ are reported. Notice that the fit is accurate only in the vicinity of the design frequency f_d.

The 2 linear operators $\mathcal{L}_\pm$ are fitted to the linearization (8) of $Q_\pm$, which are defined in (5). Since this is a fitting algorithm, the fitted operators $\mathcal{L}^{\text{fit}}_\pm$ are affected by error, and the equation (8) holds only in an approximate sense. In particular, also the phase responses $\varphi^{\text{fit}}_\pm$ are not exactly in quadrature, with equations (7) valid only in an approximate sense. We can however take this into account and calculate the nonlinear saturations $\mathcal{N}_\pm$ as the projections of the original operator Q on these slightly non-orthonormal operators, as discussed in section 2.4.

2.3.1 The design phase

This paragraph discusses a technicality regarding the choice of the design phase $\overline{\varphi}_d$. We observe that the value of $L_\pm(\omega_d)$ depends both on the linear gain $G(0,\omega)$ and on the phase response $\overline{\varphi}_d$ of $Q_\pm$. A geometric interpretation is immediate in figure 2. For example, if the linear response (black vector, top-right quadrant) is very close to the direction of Q_-, then its projection on Q_+ will be small, and the gain of L_+ will be small as well from (8). This situation can lead to a very small linear gain and a very steep nonlinear response; in the worst case, if $L_+(\omega) = 0$ the model would be flawed, as the nonlinear response $N[L[u]]$ would be zero not just in the linear regime but at all amplitudes. We can avoid these situations by choosing an appropriate value for $\overline{\varphi}_d$. Among the many possibilities, we choose to first calculate the design phase as $\overline{\varphi}_d = \overline{\varphi(\omega_d, A)}$, averaged over the possible forcing amplitudes A at the design frequency. Geometrically, it represents the orientation of the dashed line that best represents the average orientation of the output vectors in the top-right quadrant of figure 2. If then such line is too close to the direction of one of the operators $Q_\pm$, i.e. if $|\overline{\varphi}_d \pm \pi/4 - \varphi(\omega_d, 0)| < \pi/8$, we suitably add or subtract to it an angle $\pi/8$.

2.4 Nonlinear operator fitting

We fitted in the previous section the linear operators $\mathcal{L}^{\text{fit}}_\pm$ of the 2 Hammerstein models $Q_\pm$. In this section we fit the nonlinear operators $\mathcal{N}_\pm$, that are defined in the frequency domain by the approximation (11). We now treat it as an equality at the design frequency ω_d:

$$Q(A,\omega_d) = N_-(A)L^{\text{fit}}_-(\omega_d) + N_+(A)L^{\text{fit}}_+(\omega_d) \tag{14}$$

Both sides of (14) are complex valued, and $L^{\text{fit}}_+(\omega_d)$ and $L^{\text{fit}}_-(\omega_d)$ are linearly independent phasors[4]. We then operate a vector projection in the complex plane of $Q(A,\omega_d)$ on the base composed of the 2 phasors, $\{L^{\text{fit}}_+(\omega_d)$,$L^{\text{fit}}_-(\omega_d)\}$. To do so, we use the scalar product

$$\langle a, b\rangle \equiv \Big[\text{Re}(a)\text{Re}(b) + \text{Im}(a)\text{Im}(b)\Big]\Big|_{\omega=\omega_d} \tag{15}$$

and the norm as $|a|^2 \equiv \langle a, a\rangle$. With this structure, for each value of A, the quantities $N_\pm(A)$ are the projections of $Q(A,\omega_d)$ on the 2 phasors:

$$\begin{bmatrix} N_+(A) \\ N_-(A) \end{bmatrix} = \frac{1}{|L^{\text{fit}}_-|^2|L^{\text{fit}}_+|^2 - \langle L^{\text{fit}}_-, L^{\text{fit}}_+\rangle^2} \cdot \\ \cdot \begin{bmatrix} |L^{\text{fit}}_-|^2, & -\langle L^{\text{fit}}_-, L^{\text{fit}}_+\rangle \\ -\langle L^{\text{fit}}_-, L^{\text{fit}}_+\rangle, & |L^{\text{fit}}_+|^2 \end{bmatrix} \begin{bmatrix} \langle Q(A,\omega_d), L^{\text{fit}}_+\rangle \\ \langle Q(A,\omega_d), L^{\text{fit}}_-\rangle \end{bmatrix} \tag{16}$$

Equation (16) can be obtained by applying the scalar product (15) between both sides of (14) and the two phasors one at a time, and inverting the resulting system of equations. Now the 2 nonlinear operators $\mathcal{N}_\pm$ are defined in the frequency domain by the 2 real-valued describing functions $N_\pm(A)$ evaluated in (16). In this section we show how to calculate the memory-less state-space realization $\mathcal{N}[u(t)]$ of a sinusoidal input, real-valued describing function $N(A)$. The novelty proposed here is in using a Fourier–Bessel expansion, which leads to good convergence properties, without the use of iterative algorithms as proposed in [29]. We want to choose a convenient analytical structure for $\mathcal{N}$ that is able to survive the evaluation of temporal averaging that defines the describing function in equation (1). We propose the following analytical structure for $\mathcal{N}(u)$:

$$\mathcal{N}(u) \approx q^{erf}_{\mu,\kappa}(u) + \sum_{n=1}^{N_b} c_n J_1(\hat{u}_n u) \tag{17}$$

for a suitable choice of the parameters μ, κ and of the coefficients c_n. The first term in (17) is a modified error function, defined as:

$$q^{erf}_{\mu,\kappa}(u) \equiv \kappa \text{erf}\left[\frac{\sqrt{\pi}\mu u}{2\kappa}\right] \ , \ \text{erf}(x) \equiv \frac{2}{\sqrt{\pi}}\int_0^x e^{-t^2}dt \tag{18}$$

[4] because they are approximately in quadrature

The function (18) is constructed in a way that the linear gain is μ and the output saturates at κ:

$$\left.\frac{\partial q^{erf}_{\mu,\kappa}(u)}{\partial u}\right|_{u=0} = \mu \qquad \lim_{u\to\pm\infty} q^{erf}_{\mu,\kappa}(u) = \pm\kappa \tag{19}$$

The second term in (17) is a Fourier–Bessel series. The function $J_k(x)$ is the Bessel function of the first kind of order k, and

$$\hat{u}_n = \frac{\tilde{u}_n}{W}, \tag{20}$$

where $\tilde{u}_n$ is the n-th root of $J_1(x) = 0$, with $\tilde{u}_1$ being the smallest non-zero root, and W is a scaling factor. The first derivative of (17) at the origin is

$$\beta \equiv \mu + \lim_{u\to 0}\frac{\partial}{\partial u}\left[\sum_{j=1}^{N_b} c_n J_1(\hat{u}_n u)\right] = \mu + \frac{1}{2}\sum_{n=1}^{N_b} c_n \hat{u}_n \tag{21}$$

The expansion (17) admits an analytical solution of the integral (1):

$$N(A) = \mu e^{-k^2A^2}\left[I_0(k^2A^2) + I_1(k^2A^2)\right] + 2\sum_{n=1}^{N_b}\frac{c_n}{A} J_0\left(\frac{\hat{u}_n A}{2}\right) J_1\left(\frac{\hat{u}_n A}{2}\right) \tag{22}$$

where $k \equiv \sqrt{\frac{\pi}{8}}\frac{\mu}{\kappa}$ and $I_k(x)$ is the modified Bessel function of the first kind of order k. An advantage of this series expansion over a polynomial is a much better convergence far from the origin. The proof of the identity (22) is reported in the appendix A. One can then fit the coefficients $\mu, \kappa, W, \{c_n\}$ to best approximate the known function at the LHS. First we choose to fit the modified error function term to minimize its distance to $N(A)$, obtaining the value of k and μ. Then the remaining terms are non-orthogonal functions. For a fixed value of W, the fitting of a function on a non-orthonormal base is explained in [41]. We then look for the optimal value of the scaling factor W leading to the best fit. One fitting with 40 terms of the Fourier–Bessel series is presented in figure 5, with the error reported in red on the right vertical axis. Since at small amplitudes no experimental data is available (as discussed in figure 1) the operator has a plateau close to the origin. To reduce the fitting error at the the end of the plateau where the first derivative is discontinuous, we locally applied a moving average filter around the kink before proceeding with the fitting.

The proposed analytical structure (17) has proved effective at fitting all the describing functions of the example application, with an accuracy as good as the one presented in figure 5, with usually 20 terms being sufficient to provide a good fit. The fitting presented in this subsection can be successfully used whenever one needs to accurately represent in state-space a real-valued smooth sinusoidal describing function.

2.5 The final state-space realization

This section collects the results of the previous subsections. The 2 linear operators $\mathcal{L}_\pm$ admit the state-space realization (13):

$$\begin{cases}\dot{x}_\pm(t) &= A_\pm x_\pm(t) + B_\pm u_{L\pm}(t)\\ \mathcal{Q}_\pm(t) &= C_\pm x_\pm(t) + D_\pm u_{L\pm}(t)\end{cases} \tag{23}$$

where $u_{L\pm}$ are the inputs of the 2 linear operators. The matrices describing this linear system were calculated in subsection 2.3. From equation (9b), these inputs are saturated by the nonlinear memory-less functions $\mathcal{N}_\pm$:

$$u_{L\pm} = \mathcal{N}_\pm[u(t)] \tag{24}$$

where u is the input of the final operator. The 2 nonlinear saturations $\mathcal{N}_\pm$ have the analytical structure (17), and the coefficients describing them were calculated in subsection 2.4. We can then put the 2 equations (23) and (24) together and obtain

$$\begin{cases}\dot{x}_\pm(t) &= A_\pm x_\pm(t) + B_\pm \mathcal{N}_\pm[u(t)]\\ \mathcal{Q}_\pm(t) &= C_\pm x_\pm(t) + D_\pm \mathcal{N}_\pm[u(t)]\end{cases} \tag{25a}$$

The final output is then given by (4):

$$\mathcal{Q}[u(t)] = \mathcal{Q}_-[u(t)] + \mathcal{Q}_+[u(t)] \tag{25b}$$

Equations (25) fully describe the nonlinear state-space realization, and the internal state of the operator is $\{x_+, x_-\}$. This subsection concludes the description of the nonlinear state-space realization, which will be used in section 3.2 in the example application in the time domain.

3 Application

This section presents an application example of the state-space realization. The example consists of a self-excited system, schematically represented in figure 6, where only one nonlinear operator Q is present.

In section 3.1 we study the system in the frequency domain with the harmonic balance method. In section 3.2 we study it in the time domain with the state-space realization of the describing function introduced in section 2. We compare the results obtained with the 2 techniques in 3.3.

We describe briefly the physics of the application example in the rest of this part, and later solve the problem in subsection 3.1 and 3.2.

We model the experiment [31,7] of a confined, turbulent, partially premixed swirling flame. The experiment consists schematically of three parts: *1)* the configuration upstream of the flame, which includes the

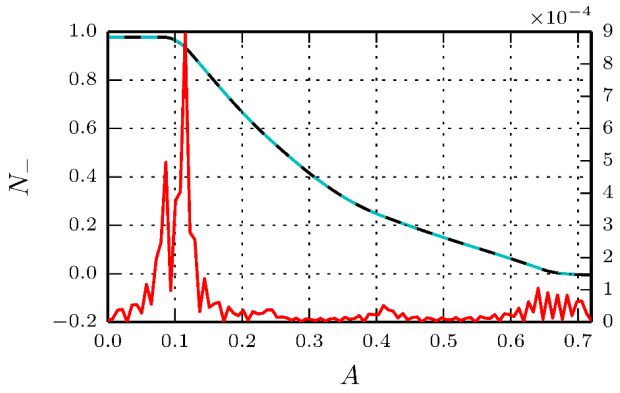

(a) Operator N_-, saturating the input for L_-

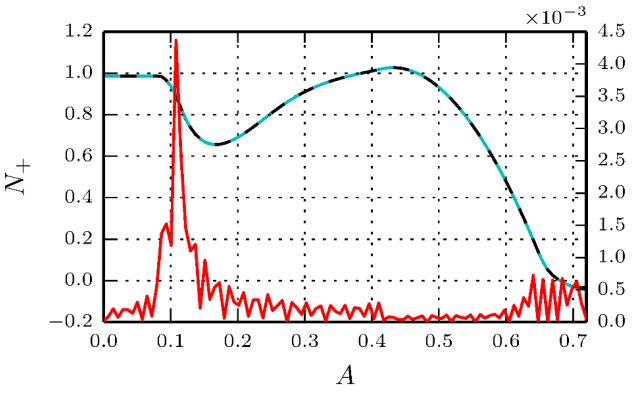

(b) Operator N_+, saturating the input for L_+

Fig. 5: Fitting of the 2 real-valued describing functions $N_-(A)$ and $N_+(A)$ at $f_l = 180\,\mathrm{Hz}$, with $N = 40$ terms in the Fourier–Bessel series. The original functions and their fit are reported respectively with a continuous black line and a dashed cyan line. They are barely distinguishable by eye, and their value is reported on the left vertical axis of each figure. The absolute value of their difference is reported in red, and refers to the vertical axis on the right.

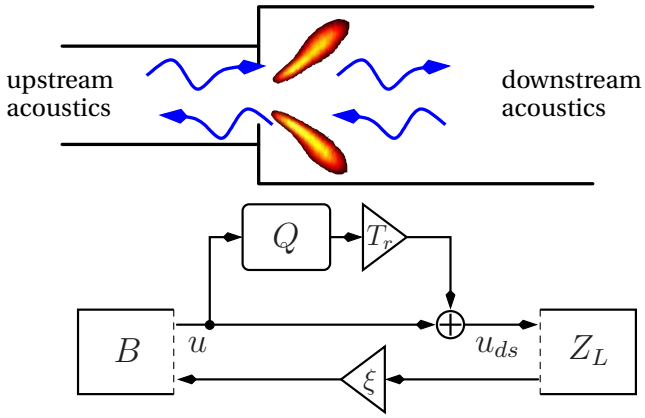

Fig. 6: Sketch of the experiment. B and Z_L are linear time-invariant operators, with L being the length of the downstream duct, which can be changed. $\xi \equiv (\rho c)_{ds}/(\rho c)_{us}$ and $T_r \equiv T_{ds}/T_{us}$ are multiplicative factors, and $Q(A,\omega)$ is the nonlinear operator considered in section 2.

burner and the swirler; *2)* the flame, assumed to be compact when compared to the length of the experiment; *3)* the exhaust gas tube of variable length L.

Since the focus of this article is on the nonlinear flame model, we do not describe in detail the configuration of the experiment, which can be found in [31,7]. The configuration upstream of the flame is fixed, and its acoustic response is governed in the frequency domain by the admittance B:

$$\hat{u} = B(\omega)\frac{\hat{p}}{(\rho c)_{us}} \tag{26}$$

where (ρc) is the characteristic impedance of the gas, i.e. the product of density and speed of sound, the latter being a function of temperature. Here and in the following, we indicate with a hat variables that depend on frequency, e.g. $\hat{u} = \hat{u}(\omega)$, and we will drop the hat to discuss time domain variables, such as $u = u(t)$. The variables $\hat{p}$ and $\hat{u}$ in (26) are measured just upstream of the flame surface and refer to acoustic pressure and velocity. We avoid adding the subscript us to both quantities to not burden the notation in the previous sections, where u can be interpreted more generally as the input of a generic nonlinear operator $\mathcal{Q}$, in contexts different from this application. We also assume that the flame is compact in space, i.e. it is an interface between the upstream and downstream geometry. In a similar manner, the acoustics downstream of the flame are described by the impedance Z_L:

$$\frac{\hat{p}_{ds}}{(\rho c)_{ds}} = Z_L(\omega)\hat{u}_{ds} \tag{27}$$

This impedance depends parametrically on the length L of the downstream duct, which can be varied. At the flame interface, under the assumption of a low Mach number flow, the pressure is continuous across the flame interface [42], i.e. $\hat{p} = \hat{p}_{ds}$, which we rewrite as:

$$\frac{\hat{p}}{(\rho c)_{us}} = \frac{(\rho c)_{ds}}{(\rho c)_{us}}\frac{\hat{p}_{ds}}{(\rho c)_{ds}} \tag{28a}$$

At the flame interface the fluctuating heat release rate induces a sudden expansion of the gas:

$$\hat{u}_{ds} = \left[1 + \left(T_{ds}/T_{us} - 1\right) Q\left(A,\omega\right)\right]\hat{u} \tag{28b}$$

The degree of this expansion depends on the ratio T_{ds}/T_{us} of the temperatures in Kelvin degrees downstream and upstream of the flame, and on the sensitivity of the fluctuating heat release rate on acoustic forcing, described by the describing function Q, which depends on the amplitude A of the upstream velocity fluctuation, with $u(t) = A\cos(\omega t)$. Equation (28b) can be derived from [43] imposing the continuity of the pressure at the surface.

All quantities describing the problem have either been directly measured or estimated in [31,7].

3.1 Frequency domain

This section evaluates the amplitude and the frequency of the limit cycles of the example problem using the harmonic balance method. Combining the equations (26,27,28) we obtain this dispersion relation in ω:

$$B(\omega)\frac{(\rho c)_{ds}}{(\rho c)_{us}}Z_L(\omega)\left[1+\left(T_{ds}/T_{us}-1\right)Q\left(A,\omega\right)\right]=1$$

The relation is parametric in the length L of the combustion chamber. For the acoustic operators B and Z_L we fit a rational function approximation as described in section 2.3, but with a number of poles $N = 12$. The rational function can then be evaluated at arbitrary values of $s = \sigma + i\omega$. On the other hand, we assume that the flame response Q is independent of the growth-rate σ, and extrude the value from the imaginary axis, calculating it according to $Q(A, \mathrm{Im}[s] = \omega)$. This leads to the dispersion relation

$$\mathcal{H}_L[\sigma,\omega,A]=0 \tag{29}$$

where

$$\begin{aligned}\mathcal{H}_L[\sigma,\omega,A] =&\mathcal{H}_L[s,A]\equiv T_L^{\mathrm{fit}}(\sigma+i\omega)\cdot\\ &\cdot\left[1+\left(T_{ds}/T_{us}-1\right)Q\left(A,\omega\right)\right]-1\end{aligned} \tag{30}$$

$$T_L^{\mathrm{fit}}(s)\equiv B^{\mathrm{fit}}(s)\frac{(\rho c)_{ds}}{(\rho c)_{us}}Z_L^{\mathrm{fit}}(s) \tag{31}$$

Equation (29) is a nonlinear eigenvalue problem in the complex Laplacian variable $s = \sigma + i\omega$.

3.1.1 Linear stability analysis

In the linear regime, the amplitude A is zero and we study the solutions of the problem $\mathcal{H}_L[\sigma, \omega, 0] = 0$. For each length L, the absolute value of $\mathcal{H}_L$ is calculated in a regular fine grid $\{\sigma_m, \omega_n\}$ in the range of interest, as reported for $L = 0.8$ in figure 7. A numerical search of the zeros of the equation is then started from the local minima of the map. These zeros are the linear eigenvalues of the problem, reported for all lengths in figure 8 in terms of growth-rates and frequencies.

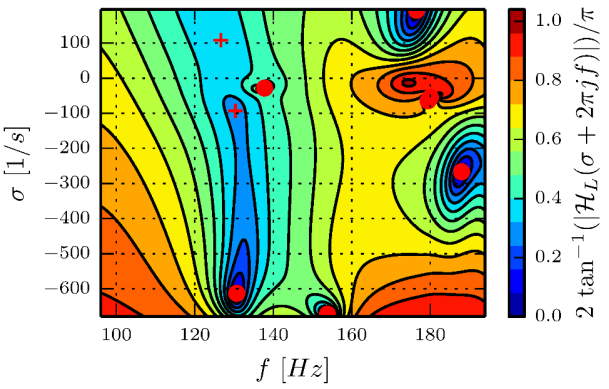

Fig. 7: absolute value of the LHS of the dispersion relation (29) describing the problem for L =0.8 m. Local minima are reported with red crosses, and solutions with red circles. Only the portion of the domain presenting solutions is shown. The value is rescaled with the arctangent function to present a finite codomain [0 , 1] for representation purposes.

3.1.2 Nonlinear stability analysis

In this section we discuss the existence and stability of limit cycles in the system. Limit cycles are found with $\mathcal{H}_L[0, \omega, A] = 0$ because they represent periodic oscillations with zero growth rate. We numerically search for them in a similar manner to the previous section, obtaining solutions (ω_j, A_j). We then numerically perturb the amplitude of oscillation to $A_j + \delta A$ and calculate the resulting perturbed eigenvalue $\delta\sigma + i(\omega_j + \delta\omega_j)$. We then apply Loeb's criterion [15], and infer that the solution is stable/unstable if $\delta\sigma_j/\delta A \lessgtr 0$, assuming that only one frequency of oscillation is present in the system. We carry out the same analysis for all lengths L of the downstream duct, and report the amplitude and the frequency of the stable/unstable limit cycles with filled/empty circles in figure 9. There is a region with multiple solutions, for L between 0.99 and 1.02 m, one approximately at 160 Hz and the other approximately at 130 Hz.

A first observation regards the points at $L = 0.99$, 1.00 m, where 2 distinct limit cycles approximately at 160 Hz and at 130 Hz coexist. In this scenario it is impossible to discuss the stability of the 2 modes without a dual-input describing function, which is not available. Loeb's criterion can be used only to provide sufficient conditions for instability.

We then focus on the mode around 130 Hz. We fix in particular L =1.00 m, with the other lengths in the region presenting a similar behaviour. We study the eigenvalues of the problem as a function of the am-

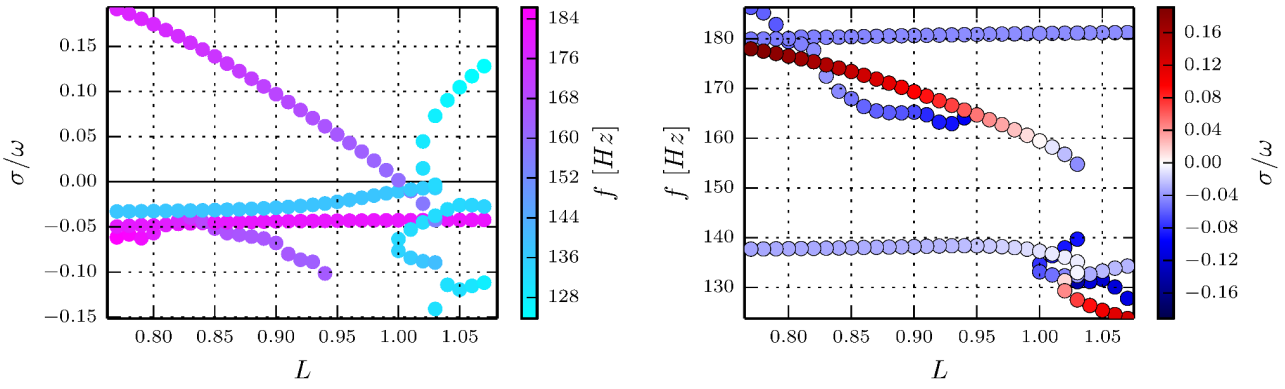

(a) Nondimensional growth-rate

(b) Frequency of oscillation

Fig. 8: Eigenvalues of the linear problem for all the lengths L of the downstream duct. The 2 plots represent the same data, using two distinct vertical axis and colormaps. In a), the height of the circles represents the growth-rate σ and the colour the frequency f of oscillation. In b), the height represents the frequency, and the colour the growth-rate. Eigenvalues with large negative growth-rate are not visible on the plot.

plitude of oscillation in figure 10. At a fixed length L in this region, there are 1 stable and 1 unstable limit cycles, at approximately the same frequency. This differs from a subcritical Hopf bifurcation, because the stable limit cycle has a smaller amplitude of oscillation then the unstable limit cycle. We also observe that if the system starts at the unstable limit cycle, it is attracted towards a higher amplitude of oscillation, until the eigenvalue disappears. It is then harder to make a definitive discussion of the nonlinear, saturated state of the system in this region. We however notice how the overall shape of the unstable mode in figure 10.a resembles a subcritical-Hopf bifurcation. The time domain analysis of the system will suggest the same behaviour.

The results from the frequency domain analysis are for the most part consistent with the experiment [7]. However, not all of the features from the present analysis could be observed in the experiment, in particular for those conditions where the analysis predicts multiple limit-cycles.

3.2 Time domain

This section evaluates the amplitude and the frequency of the limit cycles of the example problem running time domain simulations. We first combine equations (26,27,28a) and repeat (28b):

$$\hat{u} = B(\omega)\frac{(\rho c)_{ds}}{(\rho c)_{us}} Z_L(\omega)\hat{u}_{ds} \equiv T_L^{\text{fit}}(\omega)\hat{u}_{ds} \tag{32a}$$

$$\hat{u}_{ds} = \hat{u} + (T_{ds}/T_{us} - 1)\, Q\,(A, \omega)\, \hat{u} \tag{32b}$$

The operator $T_L^{\text{fit}}(\omega)$ was introduced in equation (31), and we use here its state-space representation

$$\begin{cases} \dot{x}_T(t) &= A_L x_T(t) + B_L u_{ds}(t) \\ u(t) &= C_L x_T(t) \end{cases} \tag{33a}$$

We instructed the tool VFIT3 to provide the best fit with the feedthrough matrix D_L set to 0, compare with (13). The state space model for (32b) is:

$$u_{ds}(t) = u(t) + (T_{ds}/T_{us} - 1)\, \mathcal{Q}[u(t)], \tag{33b}$$

where the operator $\mathcal{Q}$ is fully described by the equations (25). These equations can be numerically integrated in time with respect to the 3 internal state vectors $\{x_T, x_-, x_+\}$ describing respectively the acoustic state and the states of the 2 linear operators, see again (25). At each time step, $u(t)$ can be calculated with (33a), and $u_{ds}(t)$ can be calculated with (33b). Notice that if D_T was not set to 0 in (33a), an algebraic loop would appear, because $u(t)$ would depend on $u_{ds}(t)$, but also $u_{ds}(t)$ would depend on $u(t)$ because of (33b). This would require a study of the problem in the context of differential algebraic equations, with an additional root solver operation at each time step.

As initial condition $\boldsymbol{x} = \{x_T, x_-, x_+\}$ we keep generating a new random initial condition until physical values of $u_{ds}(t)$ and $u(t)$ result from (33a) and (33b). In particular, the random initial state should predict a value for the velocity u upstream of the flame such that the flame response is defined for such amplitude, and such that the gain of the nonlinear operator is in a limited range. The system is then time-integrated until it converges to a limit cycle. An example is reported in figure 11.

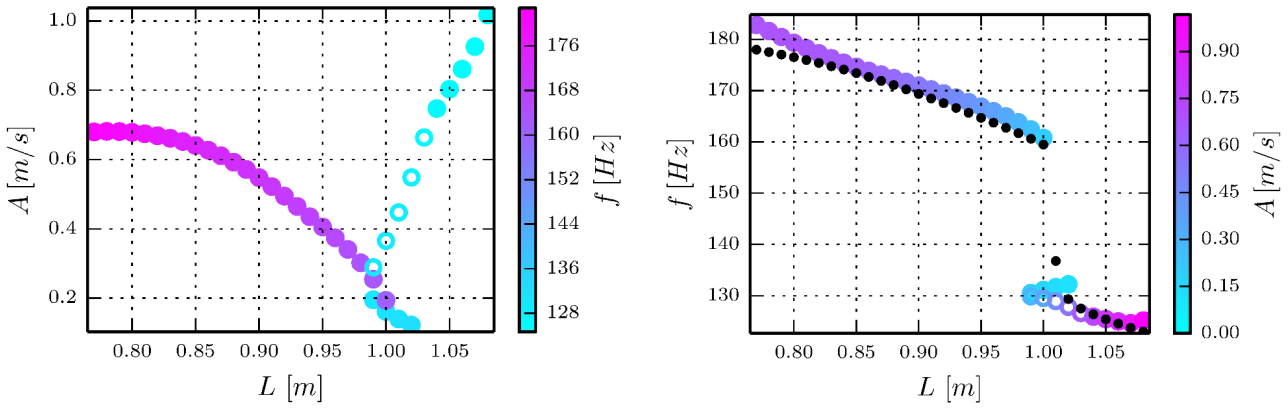

(a) limit cycle amplitude of oscillation

(b) Frequency of oscillation

Fig. 9: Nonlinear stability analysis, for all the lengths L of the downstream duct. The two plots represent the same data: in a), the height of the circles represents the limit cycle amplitude A, and the colour the frequency f of oscillation; in b), the height represents the frequency, and the colour the limit cycle amplitude A. Stable/unstable limit cycles are represented with filled/empty circles.

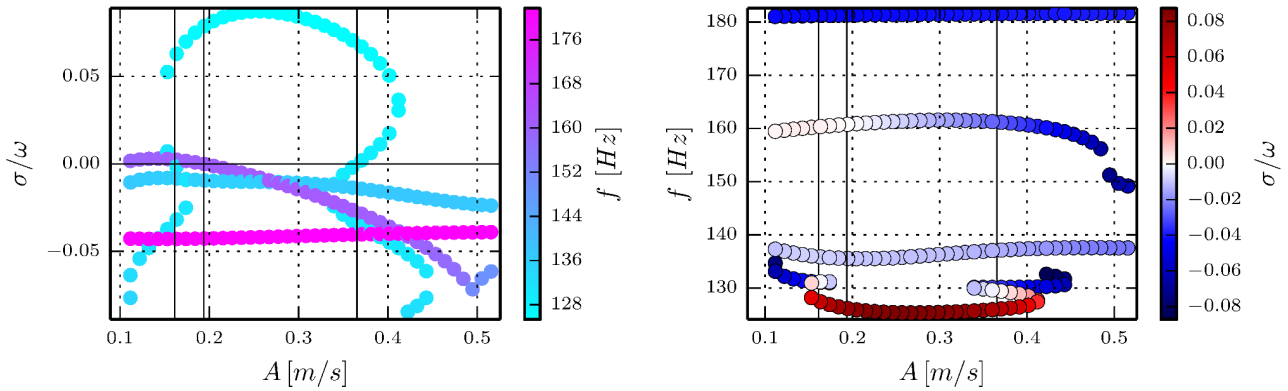

(a) Nondimensional growth-rate

(b) Frequency of oscillation

Fig. 10: Eigenvalues of the nonlinear problem for a fixed length L =1 m of the downstream duct, at discrete, equispaced amplitudes of oscillation A. The 2 plots represent the same data, using two distinct vertical axis and colormaps. In a), the height of the circles represents the growth-rate σ and the colour the frequency f of oscillation. In b), the height represents the frequency, and the colour the growth-rate. Eigenvalues with large negative growth-rate are not visible on the plot. The vertical black lines mark the amplitudes of the limit cycles, at which one growth-rate changes sign in a).

At L =1.01 m the system is linearly stable (see figure 8.a), and we tested that the system converges to the steady solution for a set of random initial conditions. Subsequently, we forced the system with an external, artificial harmonic source at the frequency of the least stable linear mode, which we stop after Δt =0.2 s. In this second case, the system converges to a stable limit cycle. This scenario describes a subcritical Hopf bifurcation.

3.3 Comparison

To compare the time domain simulations with the frequency domain simulations, we extract [44] the amplitude and the frequency of the dominant harmonic from the saturated limit cycle of $u(t)$ of each simulation, run for each value of the length L. In the first round of simulations, the design frequency ω_d is set to the frequency of the least stable mode of the linear stability analysis. These results are reported with a continuous green line in figure 12. We observe a general qualitative agreement

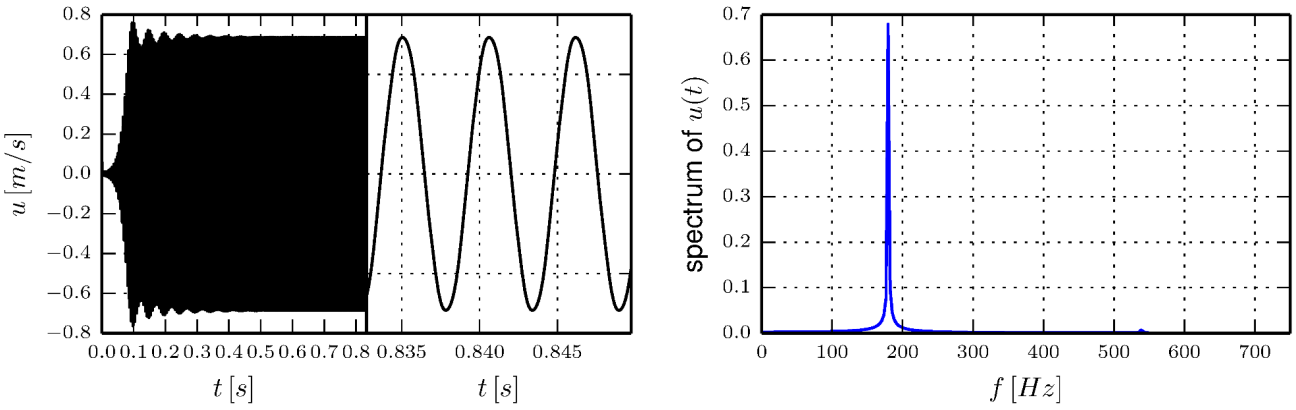

(a) velocity $u(t)$ just upstream of the flame surface

(b) Estimated power spectrum density of $u(t)$.

Fig. 11: Time simulation of the system of equations (33) for a fixed value of the length L =0.8 m of the downstream duct. a) represents the time domain signal, and b) the spectrum of the signal. The system converges to a limit cycle. The third harmonic is visible in b). Analogous simulations are carried out for all lengths L.

with the frequency domain results (coloured dots, the same as figure 9).

We also run a second round of simulations, setting ω_d to the frequency of the saturated limit cycle of the first round of simulations. We then run a third round of simulations in the same way, reported with the continuous red line in figure 12. The agreement with the frequency domain results is now much better.

We finally report the normalized difference between the 2 sets of results, in percentage, in figure 13. The error diminuishes with the number of the iteration at most points. It is larger in the transition zone discussed at the end of section 3.1.2, reported in the figure between the 2 vertical dashed lines, where the analysis in the frequency domain is harder. In particular, the error is largest at $L = 0.98$,0.99 m, where it is fundamentally not correct to compare the 2 approaches because the analysis in the frequency domain is not complete: the stability of the reported solutions can not be fully ascertained and more solutions may exist.

4 Conclusions

We present a state-space realization $\mathcal{Q}$ of a describing function Q, combining two Hammerstein models. For the linear part of the operators we use a rational function approximation, while for the nonlinear part of the model we propose the use of Fourier–Bessel series. The evaluation of the realization is fully automated and not iterative, and allows the study in the time domain of the behaviour of a system in a range of frequencies centred around a design frequency f_d.

We show the applicability of the tool on a thermoacoustic application, comparing the results of a time domain analysis using the state-space realization $\mathcal{Q}$ with the results of a nonlinear frequency-domain analysis using the original describing function Q.

In all the cases where the frequency-domain analysis is simple there is very good agreement between the results, validating the accuracy of the state-space realization proposed here.

In the other cases, the frequency-domain analysis is difficult or not possible without further information about the system. In these latter cases the state-space realization can be used as a rough tool to isolate one mode at a time, and provide quick results.

This tool will be particularly useful in the study of thermoacoustic oscillations in annular combustion chambers, where a time domain approach to the problem has so far been more successful than a frequency domain approach. It allows an accurate description of the nonlinear saturation of the problem, improving on existing time domain solvers [45,46,47].

We observe that it may be possible to change the design frequency f_d of $\mathcal{Q}$ during the time domain simulation, by extracting in real-time the instantaneous frequency of oscillation of the system and incrementally retuning the model. The extraction could be done with a nonlinear Kalman filter [48].

Acknowledgements This work was supported by the European Research Council through project ALORS N.259620 and by the German Research Association for Combustion Engines (Forschungsvereinigung Verbrennungskraftmaschinen e. V. FVV).

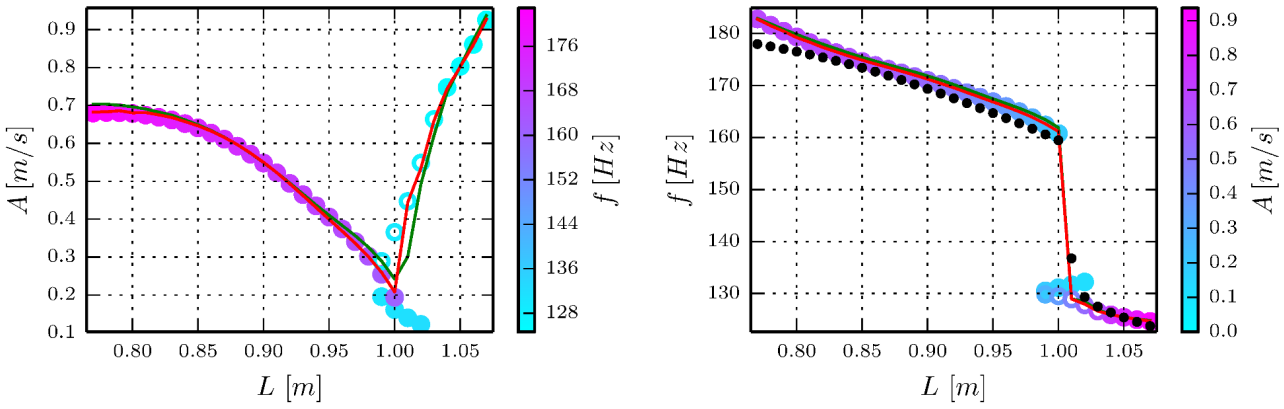

(a) Amplitude of oscillation A.

(b) Frequency of oscillation f

Fig. 12: Comparison of the results of the time domain (continuous lines) and the frequency domain (the same circles as figure 9) approaches, in terms of amplitude (in a)) and frequency of oscillation (in b)) of the saturated limit cycle. The green line is obtained with a first time simulation by setting the flame model design frequency ω_d to the frequency of the least stable linear mode (reported as black dots in b)). The red line is obtained by iterating the process 2 times.

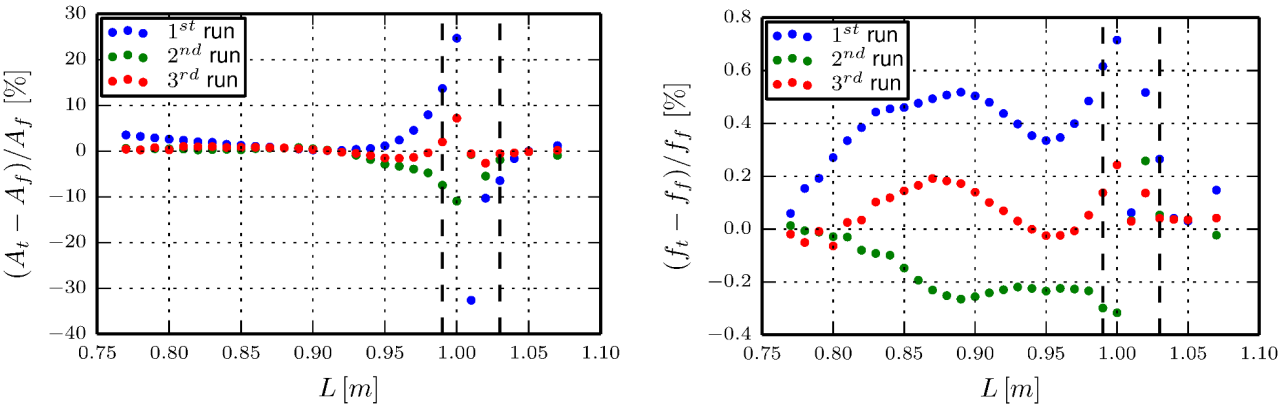

(a) Relative error for the predicted amplitude A

(b) Relative error for the predicted frequency f

Fig. 13: Error between the results obtained in the frequency domain (subscript f) and in time domain (subscript t), in percentage. The agreement is very good, except in the region where the frequency-domain stability analysis is not conclusive, delimited by the 2 vertical dashed lines.

A Describing function calculation

In this appendix we evaluate the describing function (defined by (1)) of the saturation function $\mathcal{N}$. We will prove here the more general result for an input with structure

$$u(t) = A_1 \cos(\omega t + \varphi_1) + A_2 \cos(\omega t + \varphi_2) \tag{34}$$

to the function $\mathcal{N}$, as opposed to the case under consideration in this article introduced in (1) where $u(t) = A\cos(\omega t)$. In particular, the input described by (34) describes the contribution of two modes, oscillating at the same frequency, instead of a single sinusoidal input $A\cos(\omega t+\varphi)$. The motivation to cover this more general case is to make this framework usable in rotationally symmetric annular combustors featuring azimuthal modes. In that case, each burner is subject to the combined input of two thermoacoustic modes, depending on the amplitudes A_1 and A_2 of the two modes at that location, and on their phases φ_1, φ_2. Once the result for the input (34) is obtained, it will be sufficient to set $A_1 = A$, $\varphi_1 = \varphi_2 = A_2 = 0$ to obtain the special case of the single input response used in this article, as presented at the end of the appendix.

We proceed by rewriting u as

$$u = a\cos(\omega t) + b\sin(\omega t) \tag{35}$$

by introducing the costants

$$\begin{cases} a & \equiv A_1 \cos\varphi_1 + A_2 \cos\varphi_2 \\ b & \equiv -A_1 \sin\varphi_1 - A_2 \sin\varphi_2 \end{cases} \tag{36}$$

Notice that a, b do not depend on the time variable t. We study the averaging integral in the definition (1) of describing function for the operator $\mathcal{N}$, and we will later divide by the amplitude A to recover the full expression. In other words, for the time being we study the product $N(A,\omega)A$. We substitute in the product the equation (35) and change the time variable:

$$\frac{1}{\pi}\int_0^{2\pi} \mathcal{N}\left(a\cos t + b\sin t\right)\left(\cos t + i\sin t\right) dt = f_c + i f_s \tag{37}$$

We substitute the expression for $\mathcal{N}$ from (17):

$$\begin{aligned} f_c =& \frac{1}{\pi}\int_0^{2\pi} q^{erf}_{\mu,\kappa}(a\cos t + b\sin t)\cos t dt + \\ & \sum_{n=1}^{N}\frac{c_n}{\pi}\int_0^{2\pi} J_1(\hat{u}_n(a\cos t + b\sin t))\cos t dt \\ \equiv & f_c^{erf} + \sum_{n=1}^{N} c_n f_c^{b,n} \end{aligned} \tag{38a}$$

$$\begin{aligned} f_s =& \frac{1}{\pi}\int_0^{2\pi} q^{erf}_{\mu,\kappa}(a\cos t + b\sin t)\sin t dt + \\ & \sum_{n=1}^{N}\frac{c_n}{\pi}\int_0^{2\pi} J_1(\hat{u}_n(a\cos t + b\sin t))\sin t dt \\ \equiv & f_s^{erf} + \sum_{n=1}^{N} c_n f_s^{b,n} \end{aligned} \tag{38b}$$

We study first the integrals f_c^{erf} and f_s^{erf} due to the error function in section A.1, and then each of the N integrals $f_c^{b,n}$ and $f_s^{b,n}$ of the Fourier–Bessel series in section A.2. We put together the expressions and discuss them in section A.3.

A.1 Averaging the error function

We substitute the definition of $q^{erf}_{\mu,\kappa}$ from (18) into the expression of f_c^{erf} and f_s^{erf} in (38). We obtain

$$f_c^{erf} = \frac{\kappa}{\pi}\int_0^{2\pi} \mathrm{erf}\left(\frac{\sqrt{\pi}\mu}{2\kappa}(a\cos t + b\sin t)\right)\cos t dt \tag{39a}$$

$$f_s^{erf} = \frac{\kappa}{\pi}\int_0^{2\pi} \mathrm{erf}\left(\frac{\sqrt{\pi}\mu}{2\kappa}(a\cos t + b\sin t)\right)\sin t dt \tag{39b}$$

For conciseness, we introduce the constant

$$k = \sqrt{\frac{\pi}{8}}\frac{\mu}{\kappa}, \tag{40}$$

so that the argument of the erf function is $\sqrt{2}k(a\cos t + b\sin t)$. This leads to neater expressions in the following. We proceed by expressing the argument of the exponential function as

$$a\cos t + b\sin t = R\sin(t+\psi), \tag{41}$$

where R and ψ are defined as

$$R \equiv \sqrt{a^2+b^2} \tag{42a}$$

$$\psi \equiv \arg(b+ia) \tag{42b}$$

The two integrals (39) become

$$f_c^{erf} = \frac{\kappa}{\pi}\int_0^{2\pi} \mathrm{erf}\left(\sqrt{2}kR\sin(t+\psi)\right)\cos t dt \tag{43a}$$

$$f_s^{erf} = \frac{\kappa}{\pi}\int_0^{2\pi} \mathrm{erf}\left(\sqrt{2}kR\sin(t+\psi)\right)\sin t dt \tag{43b}$$

We exploit the fact that the erf function is defined as an integral itself, and apply integration by parts to (43a):

$$\begin{aligned} f_c{}^{erf} =& \frac{\kappa}{\pi}\left[\mathrm{erf}\left(\sqrt{2}kR\sin(t+\psi)\right)\sin t\right]_0^{2\pi} - \\ & \frac{\kappa}{\pi}\frac{2}{\sqrt{\pi}}\sqrt{2}k\int_0^{2\pi} e^{-2k^2R^2\sin^2(t+\psi)} R\cos(t+\psi)\sin t dt \end{aligned} \tag{44}$$

The first term trivially vanishes. In the second, $2/\sqrt{\pi}$ is the factor present in the definition (18) of the erf function, and $\sqrt{2}k$ comes from the chain rule of the derivative of erf with respect to t, together with the term $R\cos(t+\psi)$ inside the integral. Substituting the definition of k from (40) only at its first occurrence into the second term, we can simplify:

$$\frac{\kappa}{\pi}\frac{2}{\sqrt{\pi}}\sqrt{2}k = \frac{\mu}{\pi} \tag{45}$$

We now apply a change of integration variable $t \to \chi - \psi$ to the integral (44), and because the integrand is periodic in t and then in χ, we keep the same limits of integration in the new variable.

$$f_c^{erf} = -\frac{\mu}{\pi}R\int_0^{2\pi} e^{-2k^2R^2\sin^2\chi}\cos\chi\sin(\chi-\psi)d\chi \tag{46}$$

We then expand the trigonometric term $\sin(\chi-\psi)$, and take the sum out of the integral. We obtain

$$f_c^{erf} = -\mu R\left[+E_{sc}\cos\psi - E_{cc}\sin\psi\right] \tag{47a}$$

$$f_s^{erf} = -\mu R\left[-E_{sc}\sin\psi - E_{cc}\cos\psi\right] \tag{47b}$$

where we introduced the integrals

$$E_{sc} \equiv \frac{1}{\pi}\int_0^{2\pi} e^{-2k^2R^2\sin^2\chi}\cos\chi\sin\chi d\chi = 0 \tag{48a}$$

$$\begin{aligned} E_{cc} \equiv & \frac{1}{\pi}\int_0^{2\pi} e^{-2k^2R^2\sin^2\chi}\cos^2\chi d\chi = \\ & \frac{2}{\pi}\int_0^{\pi} e^{-2k^2R^2\sin^2\chi}\cos^2\chi d\chi \end{aligned} \tag{48b}$$

The first integral (48a) is zero since its integrand is odd. In (48b), we exploited the fact that the integrand has period π. We then use power reduction formulas on the terms $\sin^2\chi$ and $\cos^2\chi$:

$$\begin{aligned} E_{cc} =& \frac{2}{\pi}\int_0^{\pi} e^{-k^2R^2(1-\cos 2\chi)}\frac{1+\cos 2\chi}{2}d\chi = \\ & \frac{1}{2\pi}\int_0^{2\pi} e^{-k^2R^2(1-\cos t)}(1+\cos t)dt \end{aligned} \tag{49}$$

The integrand in (49) has period 2π and is an even function of t, so:

$$\begin{aligned} E_{cc} =& \frac{1}{\pi}\int_0^{\pi} e^{-k^2R^2+k^2R^2\cos t}(1+\cos t)dt = \\ =& e^{-k^2R^2}\left(\frac{1}{\pi}\int_0^{\pi} e^{k^2R^2\cos t}dt + \frac{1}{\pi}\int_0^{\pi} e^{k^2R^2\cos t}\cos t dt\right) \\ =& e^{-k^2R^2}\left(I_0(k^2R^2) + I_1(k^2R^2)\right) \end{aligned} \tag{50}$$

In (50), $I_0(x)$ and $I_1(x)$ are the modified Bessel functions of the first kind of the zero and first order respectively. We first substitute (50,48a) in (47), and then we substitute $R\sin\psi = a$ and $R\cos\psi = b$. We obtain:

$$f_c^{erf} = a f_{nl}^{erf}(kR) \tag{51a}$$
$$f_2^{erf} = b f_{nl}^{erf}(kR) \tag{51b}$$

with

$$f_{nl}^{erf}(kR) \equiv \mu e^{-k^2R^2}\left(I_0(k^2R^2) + I_1(k^2R^2)\right) \tag{52}$$

acting as a gain, as it multiplies the linear term in (51) and depends on the amplitude of oscillation. The two analytical expressions (51) have been compared with the numerical integration of (38) and its counterpart for a few values of μ, κ, a, b, and lead to relative errors of the order of machine precision, thus confirming their validity.

A.2 Averaging Bessel functions

The n-th term of $f_c^{b,n}$ and of $f_s^{b,n}$ in (38) are respectively

$$f_c^{b,n} \equiv \frac{1}{\pi}\int_0^{2\pi} J_1(2u_n a\cos t + 2u_n b\sin t)\cos t dt \tag{53a}$$
$$f_s^{b,n} \equiv \frac{1}{\pi}\int_0^{2\pi} J_1(2u_n a\cos t + 2u_n b\sin t)\sin t dt \tag{53b}$$

where we introduced $u_n \equiv \hat{u}_n/2$. We define $\hat{f}_j^{b,n} = f_c^{b,n} + i f_s^{b,n}$ and apply the substitution

$$z = e^{it},\ \sin t = \frac{1}{2i}\left(1 - \frac{1}{z}\right),\ \cos t = \frac{1}{2}\left(1 + \frac{1}{z}\right) \tag{54}$$

We obtain

$$\hat{f}_j^{b,n} = \frac{1}{\pi}\int_0^{2\pi} J_1\left(u_n(a-ib)z + u_n(a+ib)\frac{1}{z}\right) z dt \tag{55}$$

We now change the line integral into a contour integral in the complex plane on the circle $|z| = 1$. From (54) we have that $dt = dz/iz$, and

$$\hat{f}_j^{b,n} = \frac{1}{\pi i}\oint_{|z|=1} J_1\left(u_n(a-ib)z + u_n(a+ib)\frac{1}{z}\right) dz \tag{56}$$

The Bessel function $J_1(z)$ is an entire function, so the only singularity of $\hat{f}_j^{b,n}(z)$ is at the origin, and is of the essential type. We can then apply the residue theorem,

$$\hat{f}_j^{b,n} = \frac{1}{\pi i} 2\pi i \mathrm{Res}\left[J_1\left(u_n(a-ib)z + u_n(a+ib)\frac{1}{z}\right)\right]_{z=0} = \\ = 2\mathrm{Res}\left[G(z)\right]_{z=0} \tag{57}$$

We expand the Bessel function in $G(z)$ with its Laurent series:

$$G(z) = \sum_{m=0}\frac{(-1)^m u_n^{1+2m}}{m!(m+1)!}\left(\frac{(a-ib)z + (a+ib)/z}{2}\right)^{1+2m} \tag{58}$$

We substitute the binomial expansion of the power of the sum

$$\left(\frac{(a-ib)z + (a+ib)/z}{2}\right)^{1+2m} = \\ \frac{1}{2^{1+2m}}\sum_{k=0}^{1+2m} z^{k-(2m+1-k)}\binom{1+2m}{k}(a-ib)^k(a+ib)^{1+2m-k} \tag{59}$$

The residue in (58) is the sum of the coefficients of the term $1/z$. Therefore, in the sum (59) we retain only the term with $k-(2m+1-k) = -1$, from which follows $k = m$. This term of (59) is:

$$\frac{1}{2^{1+2m}} z^{-1}\binom{1+2m}{m}(a-ib)^m(a+ib)^{m+1} = \\ \frac{a+ib}{2}\frac{1}{2^{2m}} z^{-1}\frac{(2m+1)!}{m!(m+1)!}(a^2+b^2)^m \tag{60}$$

Equation (57) evaluates to

$$\hat{f}_j^{b,n} = (a+ib)\sum_{m=0}^{\infty}\frac{(-1)^m(2m+1)!u_n^{1+2m}}{(m!(m+1)!)^2}\left(\frac{R}{2}\right)^{2m}$$

with $R = \sqrt{a^2+b^2}$. This series converges to

$$\hat{f}_j^{b,n} = (a+ib)\frac{2J_0\left(u_n\sqrt{a^2+b^2}\right)J_1\left(u_n\sqrt{a^2+b^2}\right)}{\sqrt{a^2+b^2}} \tag{61}$$

The two forcing terms (53) can be evaluated as the real and imaginary part of (61):

$$f_c^{b,n} = a f_{nl}^{b,n}(R) \tag{62a}$$
$$f_s^{b,n} = b f_{nl}^{b,n}(R) \tag{62b}$$

where we introduced

$$f_{nl}^{b,n}(R) \equiv 2\frac{J_0(u_nR)J_1(u_nR)}{R} \tag{63}$$

A.3 Final expression

The final expression of f_c and of f_s is obtained by substituting (51) and (62) into (38):

$$f_c(a,b) = a\left(f_{nl}^{erf}(kR) + \sum_{n=1}^{N} c_n f_{nl}^{b,n}(R)\right) = a f_{nl}(R) \tag{64a}$$
$$f_s(a,b) = b\left(f_{nl}^{erf}(kR) + \sum_{n=1}^{N} c_n f_{nl}^{b,n}(R)\right) = b f_{nl}(R) \tag{64b}$$

with $u_n = \hat{u}_n/2$, the constant $k = \mu/\kappa\sqrt{\pi/8}$ as defined in (40), the value of R is defined in (42a) and

$$f_{nl}(R) \equiv f_{nl}^{erf}(kR) + \sum_{n=1}^{N} c_n f_{nl}^{b,n}(R) \tag{65}$$

where f_{nl}^{erf} and $f_{nl}^{b,n}$ have been defined respectively in (52) and (63). The two terms f_c and f_s in (64) are symmetric with respect to a, b, since we have $f_c(a,b) = f_s(b,a)$.

By exploiting the fact that $\lim_{R\to 0} J_1(R)/R = 1/2$, and then substituting (21), we observe that

$$\lim_{R\to 0} f_{nl}(R) = \mu + \sum_{j=0}^{N} c_n u_n = \mu + \frac{1}{2}\sum_{j=0}^{N} c_n\hat{u}_n \equiv \beta \tag{66}$$

where we substituted the property (21) in the last passage. It can be proved that the first derivative at zero is

$$\lim_{R\to 0}\frac{\partial f_{nl}}{\partial R}(R) = 0, \tag{67}$$

meaning that f_{nl} is constant at first order in R.

In the case of the input described by a single sinusoid $A\cos(\omega t)$, it is sufficient to set $A_1 = A$, $\varphi_1 = \varphi_2 = A_2 = 0$. This leads in the definitions in (36) to $a = A, b = 0$, and the substitution of these in (64) leads to

$$f_c(a,b) = A\left(f_{nl}^{erf}(kA) + \sum_{n=1}^{N} c_n f_{nl}^{b,n}(A)\right) = A f_{nl}(A) \quad (68a)$$

$$f_s(a,b) = 0 \quad (68b)$$

The component in quadrature with the input signal u is zero, and $N(A)$ is real valued. Substituting (68) in (37), and because (37) is equal to $N(A,\omega)A$, we obtain

$$N(A,\omega) = f_{nl}(A) \quad (69)$$

with f_{nl} matching the RHS of (22).

References

1. T. Lieuwen, V. Yang, *Combustion Instabilities In Gas Turbine Engines* (American Institute of Aeronautics and Astronautics, Reston ,VA, 2005). DOI 10.2514/4.866807. URL http://arc.aiaa.org/doi/book/10.2514/4.866807
2. T. Lieuwen, *Unsteady Combustor Physics* (Cambridge University Press, Cambridge, 2012). DOI 10.1017/CBO9781139059961. URL http://ebooks.cambridge.org/ref/id/CBO9781139059961
3. A.P. Dowling, Journal of Fluid Mechanics **346**, 271 (1997)
4. N. Noiray, D. Durox, T. Schuller, S. Candel, Journal of Fluid Mechanics **615**(2008), 139 (2008). DOI 10.1017/S0022112008003613. URL http://www.journals.cambridge.org/abstract_S0022112008003613
5. P. Palies, D. Durox, T. Schuller, S. Candel, Combustion and Flame **158**(10), 1980 (2011). DOI 10.1016/j.combustflame.2011.02.012. URL http://linkinghub.elsevier.com/retrieve/pii/S0010218011000666
6. S. Schimek, J.P. Moeck, C.O. Paschereit, Journal of Engineering for Gas Turbines and Power **133**(10), 101502 (2011). DOI 10.1115/1.4002946. URL http://gasturbinespower.asmedigitalcollection.asme.org/article.aspx?articleid=1429530
7. B. Ćosić, J.P. Moeck, C.O. Paschereit, Combustion Science and Technology **186**(6), 713 (2014). DOI 10.1080/00102202.2013.876420. URL http://www.tandfonline.com/doi/abs/10.1080/00102202.2013.876420
8. C. Armitage, R. Balachandran, E. Mastorakos, R. Cant, Combustion and Flame **146**(3), 419 (2006). DOI 10.1016/j.combustflame.2006.06.002. URL http://linkinghub.elsevier.com/retrieve/pii/S0010218006001520
9. S. Hemchandra, Combustion and Flame **159**(12), 3530 (2012). DOI 10.1016/j.combustflame.2012.08.003. URL http://linkinghub.elsevier.com/retrieve/pii/S0010218012002301
10. H.J. Krediet, C.H. Beck, W. Krebs, S. Schimek, C.O. Paschereit, J.B.W. Kok, Combustion Science and Technology **184**(7-8), 888 (2012). DOI 10.1080/00102202.2012.663981. URL http://www.tandfonline.com/doi/abs/10.1080/00102202.2012.663981
11. L. Tay-Wo-Chong, S. Bomberg, A. Ulhaq, T. Komarek, W. Polifke, Journal of Engineering for Gas Turbines and Power **134**(2), 021502 (2012). DOI 10.1115/1.4004183. URL http://gasturbinespower.asmedigitalcollection.asme.org/article.aspx?articleid=1429715
12. B. Zinn, Journal of Sound and Vibration **13**(3), 347 (1970). DOI 10.1016/S0022-460X(70)80023-2. URL http://linkinghub.elsevier.com/retrieve/pii/S0022460X70800232
13. V. Bellucci, P. Flohr, C.O. Paschereit, F. Magni, Journal of Engineering for Gas Turbines and Power **126**(2), 271 (2004). DOI 10.1115/1.1473152. URL http://gasturbinespower.asmedigitalcollection.asme.org/article.aspx?articleid=1421769
14. B. Cosic, T.G. Reichel, C.O. Paschereit, Journal of Engineering for Gas Turbines and Power **134**(10) (2012). DOI 10.1115/1.4007024. URL http://gasturbinespower.asmedigitalcollection.asme.org/article.aspx?articleid=1477072
15. A. Gelb, W. Vander Velde, *Multiple input describing functions and nonlinear system design* (McGraw-Hill Book, 1968)
16. M. Basso, R. Genesio, A. Tesi, Nonlinear Dynamics **13**, 339 (1997)
17. J.P. Moeck, C.O. Paschereit, International Journal of Spray and Combustion Dynamics **4**(1) (2012)
18. F. Boudy, D. Durox, T. Schuller, S. Candel, Comptes Rendus Mécanique **341**(1-2), 181 (2013). DOI 10.1016/j.crme.2012.10.014. URL http://linkinghub.elsevier.com/retrieve/pii/S1631072112001787
19. L. Kabiraj, R.I. Sujith, P. Wahi, Journal of Engineering for Gas Turbines and Power **134**(3), 031502 (2012). DOI 10.1115/1.4004402. URL http://gasturbinespower.asmedigitalcollection.asme.org/article.aspx?articleid=1429767
20. K. Kashinath, I.C. Waugh, M.P. Juniper, Journal of Fluid Mechanics (2014)
21. V. Lanza, M. Bonnin, M. Gilli, IEEE Transactions on Circuits and Systems II: Express Briefs **54**(4), 343 (2007). DOI 10.1109/TCSII.2006.890406. URL http://ieeexplore.ieee.org/lpdocs/epic03/wrapper.htm?arnumber=4155062
22. B. Schuermans, C.O. Paschereit, P. Monkewitz, in *44th AIAA Aerospace Sciences Meeting and Exhibit* (American Institute of Aeronautics and Astronautics, Reston, Virginia, 2006). DOI 10.2514/6.2006-549. URL http://arc.aiaa.org/doi/abs/10.2514/6.2006-549
23. J. Sanders, F. Verhulst, *Averaging Methods in Nonlinear Dynamical Systems*, *Applied Mathematical Sciences*, vol. 59, 2nd edn. (Springer New York, New York, NY, 2007). DOI 10.1007/978-0-387-48918-6. URL http://www.springerlink.com/index/10.1007/978-0-387-48918-6
24. J. Kevorkian, J. Cole, *Multiple scale and singular perturbation methods* (Springer, 1996)
25. N. Noiray, M.R. Bothien, B. Schuermans, Combustion Theory and Modelling **15**(5), 585 (2011). DOI 10.1080/13647830.2011.552636. URL http://www.tandfonline.com/doi/abs/10.1080/13647830.2011.552636
26. N. Noiray, B. Schuermans, Proceedings of the Royal Society A: Mathematical, Physical and Engineering Sciences **469** (2013). DOI 10.1098/rspa.2012.0535. URL http://rspa.royalsocietypublishing.org/content/469/2151/20120535
27. G. Ghirardo, M. Juniper, Proceedings of the Royal Society A: Mathematical, Physical and

Engineering Sciences **469** (2013). URL http://rspa.royalsocietypublishing.org/content/469/2157/20130232.short
28. J.H. Taylor, in *American Control Conference* (1983)
29. A. Nassirharand, Advances in Engineering Software **40**(8), 600 (2009). DOI 10.1016/j.advengsoft.2008.11.003. URL http://linkinghub.elsevier.com/retrieve/pii/S0965997808001919
30. E. Eskinat, S.H. Johnson, W.L. Luyben, AIChE Journal **37**(2), 255 (1991). DOI 10.1002/aic.690370211. URL http://doi.wiley.com/10.1002/aic.690370211
31. B. Cosic, J.P. Moeck, C.O. Paschereit, Proceedings of ASME Turbo Expo 2013 pp. 1–11 (2013)
32. P. Dierckx, *Curve and Surface Fitting with Splines* (Oxford University Press, 1993)
33. J.C. Gómez, E. Baeyens, Journal of Process Control **14**(6), 685 (2004). DOI 10.1016/j.jprocont.2003.09.010. URL http://linkinghub.elsevier.com/retrieve/pii/S0959152403001173
34. T. Schuller, D. Durox, S. Candel, Combustion and Flame **134**(1-2), 21 (2003). DOI 10.1016/S0010-2180(03)00042-7. URL http://linkinghub.elsevier.com/retrieve/pii/S0010218003000427
35. B. Gustavsen, A. Semlyen, IEEE transactions on Power Delivery **14**(3), 1052 (1999)
36. B. Gustavsen, S. Member, IEEE transactions on Power Delivery **21**(3), 1587 (2006)
37. S. Kurokawa, F.N.R. Yamanaka, A.J. Prado, J. Pissolato, Electric power systems research **79**, 1155 (2009). DOI 10.1016/j.epsr.2009.02.007
38. M.R. Bothien, J.P. Moeck, A. Lacarelle, C.O. Paschereit, Proceedings of the Institution of Mechanical Engineers, Part A: Journal of Power and Energy **221**(5), 657 (2007). DOI 10.1243/09576509JPE384. URL http://pia.sagepub.com/lookup/doi/10.1243/09576509JPE384
39. B. Gustavsen, IEEE transactions on Power Delivery **23**(4), 2278 (2008)
40. B. Gustavsen, C. Heitz, IEEE Transactions on advanced packaging **31**(4), 664 (2008)
41. W. Klink, G. Payne, Journal of Computational Physics **21**, 208 (1976)
42. T. Lieuwen, Journal of Propulsion and Power **19**(5), 765 (2003). DOI 10.2514/2.6193. URL http://arc.aiaa.org/doi/abs/10.2514/2.6193
43. B. Schuermans, W. Polifke, C.O. Paschereit, ASME, International Gas Turbine and Aeroengine Congress and Exhibition, Indianapolis, IN (1999)
44. A. Choi, IEEE Transactions on Speech and Audio Processing **5**(2), 201 (1997). DOI 10.1109/89.554783. URL http://ieeexplore.ieee.org/lpdocs/epic03/wrapper.htm?arnumber=554783
45. C. Pankiewitz, T. Sattelmayer, Journal of Engineering for Gas Turbines and Power **125**(3), 677 (2003). DOI 10.1115/1.1582496. URL http://gasturbinespower.asmedigitalcollection.asme.org/article.aspx?articleid=1421647
46. B. Schuermans, V. Bellucci, C.O. Paschereit, Proceedings of ASME Turbo Expo 2003 (2003)
47. S.R. Stow, A.P. Dowling, Journal of Engineering for Gas Turbines and Power **131**(3), 031502 (2009). DOI 10.1115/1.2981178. URL http://link.aip.org/link/JETPEZ/v131/i3/p031502/s1&Agg=doi
48. H. Hajimolahoseini, M.R. Taban, H. Soltanian-Zadeh, Measurement **45**(1), 126 (2012). DOI 10.1016/j.measurement.2011.09.008. URL http://linkinghub.elsevier.com/retrieve/pii/S0263224111003034